First-principles calculations of the ultralow thermal conductivity in two-dimensional group-IV selenides

Peng-Fei Liu,[1,2,3] Tao Bo,[1,2] Juping Xu,[1,2] Wen Yin,[1,2] Junrong Zhang,[1,2] Fangwei Wang,[2,4] Olle Eriksson,[5] and Bao-Tian Wang[1,2,3,*]

[1]*Institute of High Energy Physics, Chinese Academy of Sciences (CAS), Beijing 100049, China*

[2]*Dongguan Neutron Science Center, Dongguan 523803, China*

[3]*Collaborative Innovation Center of Extreme Optics, Shanxi University, Taiyuan, Shanxi 030006, China*

[4]*Beijing National Laboratory for Condensed Matter Physics, Institute of Physics, Chinese Academy of Sciences, Beijing 100080, China*

[5]*Department of Physics and Astronomy, Division of Materials Theory, Uppsala University, Box 516, SE-75120 Uppsala, Sweden*

(Received 23 September 2018; revised manuscript received 6 December 2018; published 21 December 2018)

Through first-principles calculations, we report on the phonon-limited transport properties of two-dimensional (2D) hexagonal MSe (M = Ge, Sn, and Pb) compounds, which can be seen as a new family of 2D group-IV selenides established by the isovalent substitutions of germanium and tellurium in layered Ge_4Se_3Te phase [Angew. Chem. Inter. Edit. **56** 10204 (2017)]. We find that 2D PbSe exhibits low values of sound velocity (800–2030 m/s), large Grüneisen parameters (∼1.93), low-lying optical modes (∼20.02 cm^{-1}), and strong optical-acoustic phonon coupling. These intrinsic properties mainly stem from strong phonon anharmonicity, which greatly suppress the phonon transport and therefore give rise to an ultralow thermal conductivity (∼0.26 $W\,m^{-1}\,K^{-1}$) for 2D PbSe at room temperature. Our studies may offer perspectives for applications of thermoelectricity and motivate further experimental efforts to synthesize MSe compounds.

DOI: 10.1103/PhysRevB.98.235426

I. INTRODUCTIONS

Thermoelectricity provides a promising route for converting waste thermal energies into useful electrical energies directly, which is of great significance for energy harvesting. In general, the conversion efficiency of thermoelectric materials can be characterized by the well-defined figure of merit [1,2],

$$ZT = \frac{\sigma S^2 T}{\kappa_e + \kappa_L}, \tag{1}$$

where S, T, σ, κ_e, and κ_L are Seebeck coefficient, temperature, electric conductivity, electronic thermal conductivity, and lattice thermal conductivity, respectively. The common strategies to increase ZT mainly focus on optimizing electrical transport property (S, σ) by band-structure engineering [3] and/or reducing the heat transfer ability ($\kappa_e + \kappa_L$) through alloying and nanostructuring [4,5]. Meanwhile, screening materials with intrinsically low thermal conductivity is another important trend [6]. This method helps people to simplify complex thermoelectric parameters and focus on the optimization of electrical transport properties alone [7]. Usually, κ_L of a crystalline material can be simply evaluated by the Slack theory [8,9],

$$\kappa_L = A\frac{\bar{M}\Theta^3\delta n^{1/3}}{\gamma^2 T}, \tag{2}$$

where A is a physical constant, $\bar{M}$ is the average mass per atom in the crystal, Θ is the Debye temperature, δ is the cube root of the average volume per atom, n is the number of atoms in the primitive unit cell, and γ is the Grüneisen parameter. Obviously, seeking materials with large average atomic mass and strong anharmonicity is crucial for ideal candidates.

Theoretical and experimental studies have revealed that group IV–VI compounds have the strong anharmonicity with low κ_L [2,10–15]. For example, PbTe, a representative of medium-temperature thermoelectric material, has a very low thermal conductivity (∼2 $W\,m^{-1}\,K^{-1}$ at 300 K) [16]. The underlying microscopic mechanism mainly stems from its strong anharmonic interaction between the transverse optical and longitudinal acoustic branches [10]. *Ab initio* approaches and inelastic neutron-scattering measurements have provided important insights of the softening of the transverse optical mode affecting the κ_L [2,13–15]. Similarly in the phosphorene-like SnSe material, it has attracted intense attention for its high ZT (2.6 ± 0.3 at $T = 935$ K) and the intrinsically ultralow thermal conductivity (0.25 $W\,m^{-1}\,K^{-1}$) [17]. The intrinsic heat-conducting property in phosphorene-like SnSe has been revealed via theoretical calculations and experiment by strong anharmonicity in terms of large Grüneisen parameters. Such features could be ascribed to the weak Sn-Se atomic bonds [11,12,17]. With the outstanding electrical transport properties [7], the simple material SnSe really surprises the scientific community as a promising thermoelectric material [18–20].

Recently, the single crystal structure of Ge_4Se_3Te has been experimentally refined [21], although the hexagonal phase for $GeSe_{1-x}Te_x$ with $0.1 \leqslant x \leqslant 0.5$ was first reported in the 1960s by Muir and Cashman [22]. Different from the conventional GeSe polymorphs [23], the refined Ge_4Se_3Te phase crystallizes in the hexagonal space group with a stack of two Q-Ge-Ge-Q layers (with Q being Se and Te in a 3:1 ratio) in one unit. This reveals a novel layered material with

*Corresponding author: wangbt@ihep.ac.cn

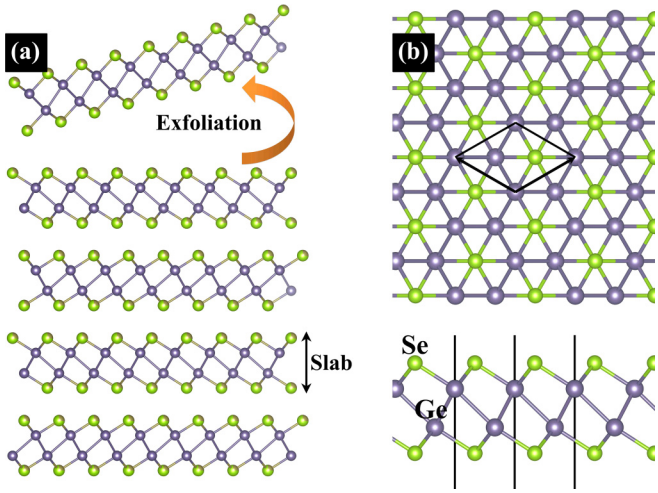

FIG. 1. (a) Schematic representation of the exfoliation process for Ge_4Se_3Te [21]. (b) Top and side views of a GeSe monolayer.

van der Waals– (vdW) type interactions and initially unexpected Ge-Ge contacts. Like the quintuple layers in Bi_2Te_3, the layered Ge_4Se_3Te could be separated from its bulk counterpart by vdW gaps via mechanical cleavage technique, as already quantified by previous density-functional-theory (DFT) results [Fig. 1(a)] [21,24,25]. In this work, by utilizing DFT methods combined with the Boltzmann transport equation, we systematically investigate phonon transport properties and lattice thermal conductivities of single-layered GeSe, SnSe, and PbSe, which can be exfoliated from the hypothetical congeners of the Ge_4Se_3Te phase. Detailed analyses of phonon spectrums, phonon density of states, phonon velocity, Debye temperatures, Grüneisen parameters, and phonon lifetimes are performed to help explain the ultralow thermal conductivity in these two-dimensional (2D) systems. The present study on their thermal transport properties is believed to unveil the promise for thermoelectric applications and motivate future experimental studies.

II. COMPUTATIONAL METHODS

First-principles calculations were performed within the framework of the Perdew-Burke-Ernzerhof [26] generalized gradient approximation [27,28], as implemented in the Vienna *ab initio* simulation package (VASP) [29]. The cutoff energy of plane wave was 500 eV on the $11 \times 11 \times 1$ Monkhorst-Pack k-point mesh. The length of the unit cell of 20 Å along the z direction was used to get rid of the interaction between adjacent images. All geometry structures were fully relaxed until the residual forces on each atom were less than 0.01 eV/Å. Employing $3 \times 3 \times 1$ and $4 \times 4 \times 1$ supercells for GeSe (SnSe) and PbSe, the phonons were calculated within the harmonic approximation via the finite-displacement method [30] using the Phonopy code [31].

In general, anharmonic behavior comes mostly from higher-order terms in the interatomic force constants, which strongly affects the acoustic phonons and dominates the heat transport [32]. It is important to describe the phonon behavior by capturing the complete anharmonicity to all orders in the case of extremely anharmonic materials [32,33]. However, in determining the thermal conductivity, for most crystals the fourth- and higher-order terms can be ignored [34–36]. Herein based on the third-order anharmonic interatomic force constants (IFCs), we studied the κ_L of single-layered GeSe, SnSe, and PbSe by solving the linearized phonon Boltzmann transport equation with the single-mode relaxation-time approximation in Phono3py [37] as below:

$$\kappa_L = \sum_{\lambda}^{3N} \int_{\mathbf{q}} \upsilon_{i,\mathbf{q}}^2 c_{i,\mathbf{q}} \tau_{i,\mathbf{q}} \mathrm{d}\mathbf{q}, \tag{3}$$

where $\upsilon_{i,\mathbf{q}}$, $c_{i,\mathbf{q}}$, and $\tau_{i,\mathbf{q}}$ are the phonon group velocity, the mode-specific heat capacity, and the relaxation time, respectively, for the ith phonon mode at the wave-vector $\mathbf{q}$ point. The third-order anharmonic IFCs on the $3 \times 3 \times 1$ supercell of 2D MSe were carried out in the VASP package with the same pseudopotentials and cutoff energy of plane-wave basis. Meanwhile, we used default setting for the cutoff pair distance, which meant full elements of third-order anharmonic IFCs were computed. There were 1260 supercells with displaced atoms that needed to be calculated for each compound. To accurately compute the κ_L, the reciprocal spaces were sampled with a $200 \times 200 \times 1$ mesh.

III. RESULTS AND ANALYSIS

A. Crystal structure and cleavage energy

Bulk Ge_4Se_3Te has been known since the 1960s [22] and was refined in 2017 [21] as the layered material with vdW type interactions and initially unexpected Ge-Ge contacts. Since the monolayer materials can be obtained using micromechanical cleavage [38–40] from their bulk vdW counterparts, the Ge_4Se_3Te monolayer may also be exfoliated from its bulk [Fig. 1(a)]. The possibility of producing GeSe, SnSe, and PbSe sheets is also estimated by peeling off the top layer from the bulk materials. Figure 1(b) shows the crystal structure of GeSe monolayer. It displays a hexagonal lattice and contains two formula units in each unit cell. This system possesses inversion symmetry. The optimized lattice constants are 3.81, 4.09, and 4.18 Å for GeSe, SnSe, and PbSe sheets, respectively. More details about the monolayered structures are listed in Table I.

To advance the feasibility of exfoliating sheets from the bulk counterparts, the cleavage energies (E_{cl}), defined as the minimum energy required to exfoliate a monolayer from bulk [41], are calculated by introducing a fracture in the bulk materials. To simulate the exfoliation process, we used a five-slab model to mimic a bulk material and calculated the energy increase as a monolayer is exfoliated from the slab. A vacuum layer (larger than 15 Å) is incorporated into the five-layer slab to avoid the artificial interaction between two neighboring slabs. The vdW forces are described by employing dispersion-corrected DFT methods, including the zero damping DFT-D3 method of Grimme (zero-damping) [42], the DFT-D3 method with Becke-Jonson damping (BJ-damping) [43], the Tkatchenko-Scheffler method (DFT-TS) [44], and the Tkatchenko-Scheffler method with iterative Hirshfeld partitioning (TSiHp) [45,46], which could provide a good description of the vdW materials [47,48]. The calculated E_{cl} of GeSe, SnSe, and PbSe sheets are about 0.21–0.25,

TABLE I. The calculated lattice parameters lattice constants (l_a in Å), bond lengths of M-Se ($l_{\mathrm{M-Se}}$ in Å) and M-M ($l_{\mathrm{M-M}}$ in Å), average atomic mass $\overline{M}$, mass ratio m_M/m_{Se}, and cleavage energy (E_{cl} in J m^{-2}) for GeSe, SnSe, and PbSe sheets, respectively.

Comp.	l_a	$l_{\mathrm{M-Se}}$	$l_{\mathrm{M-M}}$	$\overline{M}$	m_M/m_{Se}	E_{cl} (zero-damping)	E_{cl} (BJ-damping)	E_{cl} (DFT-TS)	E_{cl} (TSiHp)
GeSe	3.81	2.58	2.95	75.80	0.92	0.23	0.25	0.22	0.21
SnSe	4.09	2.76	3.32	98.84	1.50	0.27	0.29	0.26	0.24
PbSe	4.18	2.84	3.82	143.08	2.62	0.36	0.38	0.31	0.30

0.24–0.29, and 0.30–0.38 J m^{-2}, respectively. It is noteworthy that the calculated cleavage energies of MSe are comparable to that of graphite (0.37 J m^{-2}) [49], suggesting high plausibility to extract a MSe monolayer from the bulk in future experiments.

B. Phonon spectrum

The phonon dispersions and partial atomic phonon density of states (PhDOS) of GeSe, SnSe, and PbSe monolayers are shown in Fig. 2. The phononic $k\cdot$ theorem is used to sort the phonon branches according to the continuity of their eigenvectors [50–52]

$$\left|\sum e^*_{k,\sigma_1}(j)\cdot e_{k+\triangle,\sigma_2}(j)\right| = |\delta_{\sigma_1,\sigma_2} - o(\triangle)|, \qquad (4)$$

where $e^*_{k,\sigma}(j)$ is the displacement of the atom j in the eigenvector of (k,σ) vibrational mode and $\triangle$ is a small wave vector. The real frequencies of all modes in the BZ indicate that the three 2D crystals are all kinetically stable.

Since the acoustic modes are mainly responsible for heat transport in narrow gap semiconductors, we highlight these modes with different colors while the eight optical modes are black in the plots. As shown in Fig. 2, the two transverse (TA/TA′) and one longitudinal acoustic (LA) branches of GeSe, SnSe, and PbSe monolayers cross each other in the BZ, which is same to the single-layer MoS_2 [50]. The three acoustic branches of GeSe and PbSe sheets are linear near the Γ point, while the acoustic branches of PbSe show a complex trend. For the optical branches, it can be clearly seen that wide phonon gaps of 23.33, 29.64, and 65.44 cm^{-1} for GeSe, SnSe, and PbSe separate optical phonon modes into high-energy and low-energy areas. The low-energy optical branches below phonon gaps are softening and overlapping with the acoustic branches for the three sheets, leading to

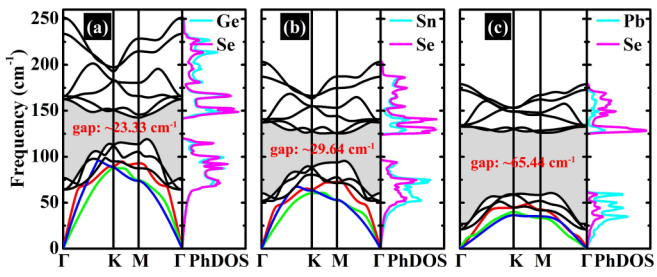

FIG. 2. Phonon dispersions and the partial atomic phonon density of states (PhDOS) of (a) GeSe, (b) SnSe, and (c) PbSe. The red, green, and blue lines in the phonon dispersions highlight two transverse (TA/TA′) modes and one longitudinal acoustic (LA) mode. The high-symmetry k points Γ, K, and M represent (0,0,0), (−1/3,2/3,0), and (0,1/2,0), respectively.

strong acoustic-optical interactions and highly nonlinear dispersion curves. This is similar to the phosphorene-like crystal SnSe [12], which has strong anharmonic effects and ultralow thermal conductivity. As seen, the lowest optical mode boundary frequencies ($\omega_{o,\min}$) of GeSe, SnSe, and PbSe are 64.19, 52.04, and 20.92 cm^{-1} (Table II), respectively, which are comparable to that of phosphorene-like SnSe (33.07 cm^{-1}) [11], suggesting that the optical mode softening is severe in these materials, as we predicted.

From the corresponding PhDOS, it can be seen that the phonon mode mainly contains the Ge (Sn, Pb) and Se vibrations in the full-energy region, while the contributions from Se vibrations become larger when getting away from the low-energy region to the high-energy region. This is more obvious in PbSe than those in GeSe and PbSe, which means the covalent bonding characteristic weakens when going from GeSe, SnSe, to PbSe with the increasing mass, mass ratio m_M/m_{Se}, and bond lengths (Table I).

C. Phonon velocity and Debye temperatures

The phonon velocities are closely relevant to the phonon transportation of the compounds. According to the formula (3), the reduced acoustic phonon velocities would lower κ_L. Here we calculate the group velocities of phonon mode ω_i using the slope of the phonon dispersion for the three monolayers, which are given by

$$\upsilon_{i,\mathbf{q}} = \frac{\partial\omega_{i,\mathbf{q}}}{\partial\mathbf{q}}. \qquad (5)$$

Figure 3 highlights the acoustic phonon group velocities for the TA, TA′, and ZA branches with different colors. The different shapes of the acoustic phonon dispersion will lead to different group velocities $\upsilon_{\mathbf{q}}$ for GeSe, SnSe, and PbSe near the zone center. As shown in Fig. 3, large acoustic phonon velocities at Γ point for the compounds are observed, which are different from those of low-dimensional materials with quadratic trend phonon spectrums [35]. For all acoustic phonon branches, it is clearly seen that most of the group velocities become smaller and smaller from the GeSe to SnSe and to PbSe monolayer, which leads to a decreasing behavior of the κ_L. For PbSe, the two transverse and the one longitudinal phonon velocities at Γ point are 0.80, 1.22, and 2.03 km/s, respectively, which are much lower than the corresponding values of 2.13, 3.16, and 4.43 km/s for GeSe and 1.80, 2.72, and 3.60 km/s for SnSe (see Table II).

The average acoustic Debye temperatures for the GeSe, SnSe, and PbSe sheets can be determined from

$$\frac{1}{\Theta_D^3} = \frac{1}{3}\left(\frac{1}{\Theta_{\mathrm{TA}}^3} + \frac{1}{\Theta_{\mathrm{TA'}}^3} + \frac{1}{\Theta_{\mathrm{LA}}^3}\right), \qquad (6)$$

TABLE II. Summary of lowest optical frequency $\omega_{o,\min}$ in cm^{-1} at the Γ point, average transverse (TA/TA′) and longitudinal (LA) Grüneisen parameters ($\overline{\gamma}_{TA/TA'/LA}$), Debye temperatures ($\Theta_{TA/TA'/LA}$ in K), and phonon velocities ($\upsilon_{TA/TA'/LA}$ in km s^{-1}) for GeSe, SnSe, and PbSe sheets, respectively.

Comp.	$\omega_{o,\min}$	$\overline{\gamma}_{TA}$	$\overline{\gamma}_{TA'}$	$\overline{\gamma}_{LA}$	Θ_{TA}	$\Theta_{TA'}$	Θ_{LA}	υ_{TA}	$\upsilon_{TA'}$	υ_{LA}
GeSe	64.19	0.92	0.68	0.60	126.68	137.34	136.45	2.13	3.16	4.43
SnSe	52.04	0.97	1.29	0.68	87.52	96.95	105.60	1.80	2.72	3.60
PbSe	20.92	1.79	1.72	2.72	46.43	57.56	70.49	0.80	1.22	2.03

where Θ_i for each acoustic branch i (i = TA, TA′, and LA) is defined as [53]

$$\Theta_i = \omega_{i,\max}/k_B, \tag{7}$$

where $\omega_{i,\max}$ is the largest acoustic frequency of the ith acoustic mode and k_B is Boltzmann constant. The Debye temperature usually reflects the magnitude of phonon velocity [54]: The larger the phonon velocity, the higher the Debye temperature. The average Debye temperature Θ_D for PbSe is calculated to be 54.94 K, much lower than those of 133.13 K for GeSe and 95.56 K for SnSe. This is consistent with the fact that the acoustic phonon velocities of PbSe are lower than those of GeSe and SnSe (Table II). The Debye temperatures of these 2D compounds are much lower than those of graphene [55], silicene [35], and phosphorene [56]. The extremely low Debye temperature and slow speed of phonon may lead to an ultralow κ_L in PbSe sheets according to Slack's theory [8].

D. Grüneisen parameters

The Grüneisen parameter is a quantity describing the anharmonic interactions of a crystal, which is useful for analyzing the physical nature of κ_L behavior. It can be calculated directly from the relationship between phonon frequency and volume change as below [9]:

$$\gamma_{i,\mathbf{q}} = -\frac{d\ln\omega_{i,\mathbf{q}}}{d\ln V}. \tag{8}$$

Generally, large $|\gamma|$ implies strong anharmonicity, which accordingly gives rise to low κ_L. To effectively evaluate the anharmonicity, we plot the dispersion of the Grüneisen parameters of acoustic modes for MSe in Fig. 4. The most noteworthy feature of these dispersions is the unusually ultrahigh values of Grüneisen parameters for PbSe monolayers, particularly around the Γ point, which implies that the acoustic branches of PbSe monolayer are strongly anharmonic. These large-mode Gruneisen parameters at acoustic frequencies are crucial to the phonon transport in materials, because most of the heat is carried by low-frequency acoustic phonons.

The average Grüneisen parameters ($\overline{\gamma}_i$) of each acoustic dispersion are calculated by [17,53,57]

$$\overline{\gamma}_i = \frac{\sum\sqrt{\gamma_{i,\mathbf{q}}^2}}{\sum\mathbf{q}}. \tag{9}$$

For GeSe sheets, the average acoustic Grüneisen parameters are $\overline{\gamma}_{TA} = 0.92$, $\overline{\gamma}_{TA'} = 0.68$, and $\overline{\gamma}_{LA} = 0.60$, which are all less than 1 (Table II). The corresponding values for SnSe are 0.97, 1.29, and 0.68, which are larger than those of GeSe but smaller than the values (1.79, 1.72, and 2.72) of PbSe. The further averages of the acoustic Grüneisens,

$$\overline{\gamma}' = \tfrac{1}{3}(\overline{\gamma}_{TA} + \overline{\gamma}_{TA'} + \overline{\gamma}_{LA}), \tag{10}$$

are calculated to be 0.73, 0.98, and 1.93 for GeSe, SnSe, and PbSe, respectively. These values are comparable to the average Grüneisen parameters of low-lattice-thermal-conductivity compounds, such as layered phosphorene-like SnSe (2.83) [17], cubic PbTe (1.45) [8], Cu_3SbSe_4 (1.22) [54], and Cu_3SbSe_3 (2.41) [54]. This means MSe sheets also have strongly anharmonic vibrational properties. In addition, the acoustic $\overline{\gamma}'$ of PbSe is much larger than those of GeSe and SnSe, indicating that PbSe has even stronger anharmonicity and lower thermal conductivity.

E. Phonon lifetimes

According to the formula (3), the phonon relaxation time is proportional to the κ_L [37]. It can be solved numerically from the phonon linewidth $2\Gamma_i(\omega_i)$ of the phonon mode:

$$\tau_i = \frac{1}{2\Gamma_i(\omega_i)}, \tag{11}$$

where the $\Gamma_i(\omega)$ takes a form analogous to the Fermi golden rule and fully incorporated scatterings from all of the phonon

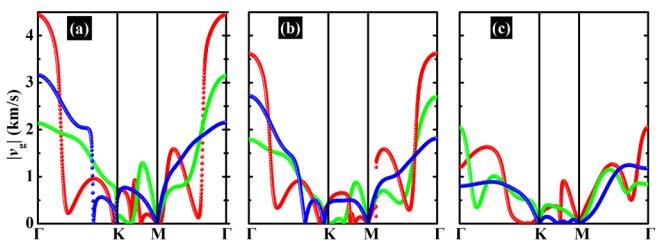

FIG. 3. The phonon mode group velocities of (a) GeSe, (b) SnSe, and (c) PbSe. The three acoustic modes are shown as red, green, and blue lines, respectively.

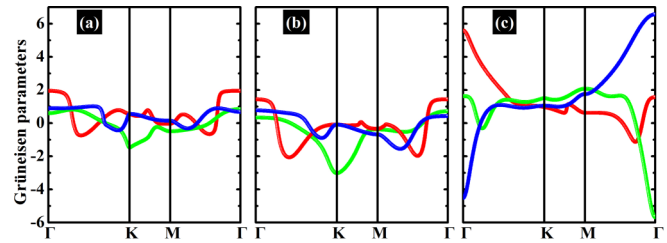

FIG. 4. Calculated Grüneisen dispersions for (a) GeSe, (b) SnSe, and (c) PbSe. The three acoustic modes are shown as red, green, and blue lines, respectively.

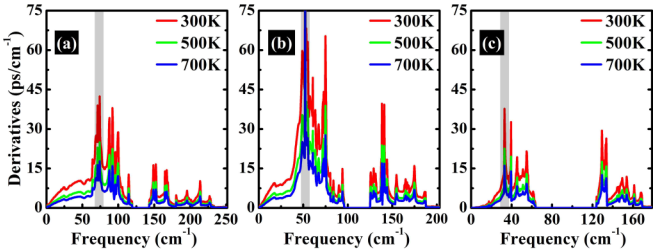

FIG. 5. The derivatives of the cumulative lifetimes with respect to frequency. Shadow region highlights the maximum peak of the derivatives.

modes [37]. Using sampling meshes in the BZ, the phonon lifetimes are calculated to be 52.27, 71.58, and 23.28 ps at 300 K. To this scope we analyze the derivatives of the cumulative phonon lifetimes with respect to frequency (Fig. 5). The shadow regions highlight the maximum peaks (73.80, 52.08, and 19.04 cm^{-1} for GeSe, SnSe, and PbSe monolayers, respectively) of the derivatives of the cumulative lifetimes. These regions dominate strong acoustic-optical interactions in the phonon spectrum. Monolayered PbSe exhibits the lowest phonon lifetimes among all our studied three monolayers. This is useful for lowering κ_L for PbSe.

F. Lattice thermal conductivity

The cumulative lattice thermal conductivities and their derivatives with respect to frequency, at 300 K, 500 K, and 700 K, are plotted in Fig. 6. The shadow regions with frequency below 119.17, 95.53, and 60.58 cm^{-1} contain the acoustic branches and low-energy optical branches. They contribute 93.26%, 90.80%, and 80.35% of the total κ_L for GeSe, SnSe, and PbSe, respectively.

With ultralow κ_L, MSe monolayers may realize high thermoelectric efficiency as new promising materials. This will motivate a systematic examination of the size dependence of thermal conductivity in these 2D materials. Here, the most simple boundary scattering treatment is adopted for the calculations. $\upsilon_{\mathbf{q}}/L$ is used as the scattering rate, where $\upsilon_{\mathbf{q}}$ and L are the group velocity and the boundary mean free path, respectively. The lattice thermal conductivities of infinite and finite-size (0.5, 0.3, 0.1, 0.05, 0.03, and 0.01 μm) monolayer GeSe, SnSe, and PbSe as a function of temperature are plotted in Fig. 7. Due to the enhanced boundary scattering [34], the lattice thermal conductivities decrease with the decreasing

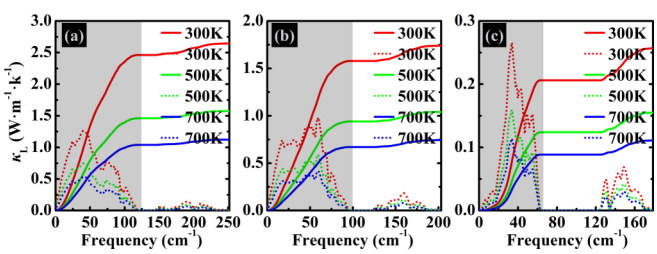

FIG. 6. The cumulative lattice thermal conductivities with respect to frequency (solid lines) and the derivatives (short dotted lines). Shadow region highlights the acoustic and low-energy optical phonon regions.

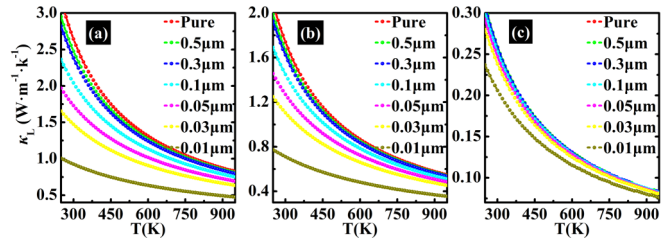

FIG. 7. The lattice thermal conductivities of infinite and finite-size (0.5, 0.3, 0.1, 0.05, 0.03, and 0.01 μm) for (a) GeSe, (b) SnSe, and (c) PbSe as a function of temperature.

sample size for the sheets. For the cases of the size being 0.1, 0.03, and 0.01 μm, the room-temperature κ_L of 2D PbSe, compared with that of the infinite case, is reduced by about 1.56%, 7.39%, and 19.84%, respectively. These are entirely lower than the corresponding values of 22.81%, 44.33%, and 65.02% for GeSe and 16.67%, 36.46%, and 59.17% for SnSe.

IV. DISCUSSIONS AND CONCLUSIONS

According to the Slack theory [8], four factors dominate the κ_L, including (i) average atomic mass, (ii) the Debye temperature, (iii) crystal structure, and (iv) anharmonicity [9]. Deduced from previous analysis, several features, including high average atomic mass, low Debye temperature, and large Grüneisen parameters, endow MSe with ultralow thermal conductivities (2.63, 1.74, and 0.26 W m^{-1} K^{-1} for GeSe, SnSe, and PbSe monolayers at 300 K). These values are similar in magnitude to those of phosphorene-like SnSe (0.62 W m^{-1} K^{-1}) [12], monolayered SbAs (1.60 W m^{-1} K^{-1}) [34], antimonene (2.59 W m^{-1} K^{-1}) [34], germanene (2.4 W m^{-1} K^{-1}) [55], dumbbell silicene (2.86 W m^{-1} K^{-1}) [35], and monolayer SnSe (3 W m^{-1} K^{-1}) [58]. Furthermore, we fit the calculated thermal conductivity with the inverse temperature ($\kappa_L \sim 1/T$), as shown in Fig. 8. It can be observed that the fitting curves follow strict linear dependence, indicating

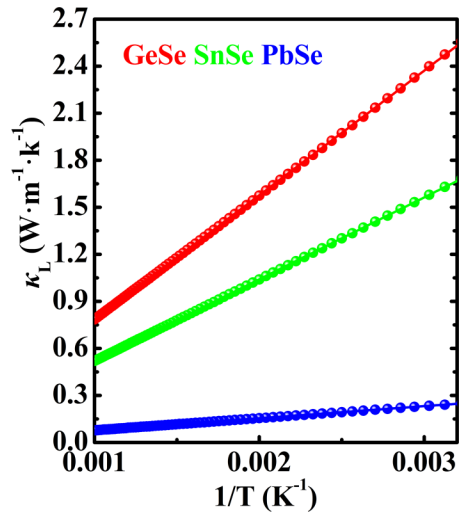

FIG. 8. Calculated lattice thermal conductivities as a function of the inverse temperature for the monolayered GeSe, SnSe, and PbSe. The fitted curves of κ_L and $1/T$ are displayed as solid lines.

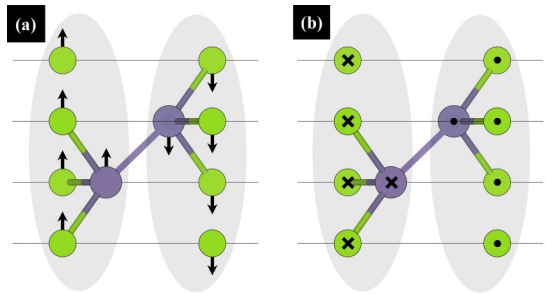

FIG. 9. The schematic diagram of the degenerate low-lying optical modes at Γ point for the monolayered MSe. The symbols · and × denote atoms moving out of and into the plane of the paper.

that the Umklapp scattering is dominant at this temperature range, which is also found in other semiconductors such as 3D PbSe [59], 3D PbTe [60], and Mg_2(Si,Sn) [61].

Previous studies have confirmed that a perfectly flat plane structure enables ultrahigh in-plane thermal conductivity for 2D layered materials [36,62]. The buckled structure can reduce the κ_L by breaking the out-of-plane symmetry, increasing anharmonic phonon scattering [55]. In the case of sandwiched structures of monolayered MoS_2, much weaker interatomic bonds in the nonplanar structures give rise to quite low group velocities and large Grüneisen parameters, which result in remarkably lower thermal conductivities [63]. For 2D MSe sheets, the unique structure with the Se-M-M-Se stacking contains buckled and sandwiched configurations simultaneously. Meanwhile, the absence of of acoustic-optical gaps greatly enhances the optical-acoustic phonon coupling in 2D MSe. DFT-based phonon spectra of the hexagonal phase at zone center (Γ point) reveal several soft optical modes with frequencies induced by the antiparallel movements of the two MSe-based planes (highlighted with shadow regions in Fig. 9). These features synergistically suppress the κ_L of 2D MSe sheets.

In summary, we report on the phonon thermal properties of 2D MSe sheets by using first-principles calculations and solving linearized the phonon Boltzmann transport equation. Calculated results show that 2D MSe sheets exhibit low κ_L, especially for monolayered PbSe. Its value of 0.26 $W\,m^{-1}\,K^{-1}$ at room temperature is even lower than that of phosphorene-like SnSe (0.62 $W\,m^{-1}\,K^{-1}$) [12]. Compared to other 2D materials, 2D PbSe shows some intrinsic factors, such as low values of sound velocity, large Grüneisen parameters, soft optical modes, and strong optical-acoustic phonon coupling. All these features can be ascribed to the strong anharmonicity of the unexpected metal contacts between layers. These results will provide a new playground for exploring materials for thermal related applications.

ACKNOWLEDGMENTS

We gratefully acknowledged the financial support from National Natural Science Foundation of China (Grants No. 11675195, No. 11675255, and No. 11634008), National Key Basic Research Program (Grant No. 2017YFA0403700), Guangdong Provincial Department of Science and Technology (Grant No. 2018A0303100013), and China Postdoctoral Science Foundation (Grant No. 2018M641477). The calculations were performed at Supercomputer Centre in China Spallation Neutron Source (CSNS).

[1] A. Majumdar, Science **303**, 777 (2004).
[2] Y. Lu, T. Sun, and D.-B. Zhang, Phys. Rev. B **97**, 174304 (2018).
[3] Y. Pei, H. Wang, and G. J. Snyder, Adv. Mater. **24**, 6125 (2012).
[4] Z. Chen, X. Zhang, and Y. Pei, Adv. Mater. **30**, 1705617 (2018).
[5] W. Kim, J. Mater. Chem. C **3**, 10336 (2015).
[6] C. Chang and L.-D. Zhao, Mater. Today Phys. **4**, 50 (2018).
[7] L.-D. Zhao, C. Chang, G. Tan, and M. G. Kanatzidis, Energy Environ. Sci. **9**, 3044 (2016).
[8] G. A. Slack, Solid State Phys. **34**, 1 (1979).
[9] L. Hou, W.-D. Li, F. Wang, O. Eriksson, and B.-T. Wang, Phys. Rev. B **96**, 235137 (2017).
[10] O. Delaire, J. Ma, K. Marty, A. F. May, M. A. McGuire, M.-H. Du, D. J. Singh, A. Podlesnyak, G. Ehlers, M. D. Lumsden, and B. C. Sales, Nat. Mater. **10**, 614 (2011).
[11] C. W. Li, J. Hong, A. F. May, D. Bansal, S. Chi, T. Hong, G. Ehlers, and O. Delaire, Nat. Phys. **11**, 1063 (2015).
[12] Y. Xiao, C. Chang, Y. Pei, D. Wu, K. Peng, X. Zhou, S. Gong, J. He, Y. Zhang, Z. Zeng *et al.*, Phys. Rev. B **94**, 125203 (2016).
[13] C. Li, O. Hellman, J. Ma, A. F. May, H. B. Cao, X. Chen, A. D. Christianson, G. Ehlers, D. J. Singh, B. C. Sales, and O. Delaire, Phys. Rev. Lett. **112**, 175501 (2014).
[14] Y. Chen, X. Ai, and C. A. Marianetti, Phys. Rev. Lett. **113**, 105501 (2014).
[15] J. W. Doak and C. Wolverton, Phys. Rev. B **86**, 144202 (2012).
[16] G. A. Akhmedova and D. S. Abdinov, Inorg. Mater. **45**, 854 (2009).
[17] L. D. Zhao, S. H. Lo, Y. Zhang, H. Sun, G. Tan, C. Uher, C. Wolverton, V. P. Dravid, and M. G. Kanatzidis, Nature **508**, 373 (2014).
[18] G. J. Snyder and E. S. Toberer, Nat. Mater. **7**, 105 (2008).
[19] C. Chang, M. Wu, D. He, Y. Pei, C.-F. Wu, X. Wu, H. Yu, F. Zhu, K. Wang, Y. Chen, L. Huang, J.-F. Li, J. He, and L.-D. Zhao, Science **360**, 778 (2018).
[20] H. Yu, W. Lao, L. Wang, K. Li, and Y. Chen, Phys. Rev. Lett. **118**, 137002 (2017).
[21] M. Küpers, P. M. Konze, S. Maintz, S. Steinberg, A. M. Mio, O. Cojocaru-Mirédin, M. Zhu, M. Müller, M. Luysberg, J. Mayer, M. Wuttig, and R. Dronskowski, Angew. Chem. Int. Ed. **56** 10204 (2017).
[22] J. Muir and R. Cashman, J. Phys. Chem. Solids **28**, 1009 (1967).
[23] A. Kuhn, A. Chevy, and R. Chevalier, Phys. Status Solidi A **31**, 469 (1975).
[24] B. Sa, Z. Sun, and B. Wu, Nanoscale **8**, 1169 (2016).
[25] Y. Ma, L. Kou, Y. Dai, and T. Heine, Phys. Rev. B **94**, 201104 (2016).
[26] G. Kresse and D. Joubert, Phys. Rev. B **59**, 1758 (1999).
[27] P. E. Blöchl, Phys. Rev. B **50**, 17953 (1994).

[28] P. E. Blöchl, O. Jepsen, and O. K. Andersen, Phys. Rev. B **49**, 16223 (1994).
[29] G. Kresse and J. Furthmüller, Phys. Rev. B **54**, 11169 (1996).
[30] S. Baroni, S. De Gironcoli, A. Dal Corso, and P. Giannozzi, Rev. Mod. Phys. **73**, 515 (2001).
[31] A. Togo, F. Oba, and I. Tanaka, Phys. Rev. B **78**, 134106 (2008).
[32] A. H. Romero, E. K. U. Gross, M. J. Verstraete, and O. Hellman, Phys. Rev. B **91**, 214310 (2015).
[33] S.-Y. Yue, X. Zhang, G. Qin, S. R. Phillpot, and M. Hu, Phys. Rev. B **95**, 195203 (2017).
[34] S.-D. Guo and J.-T. Liu, Phys. Chem. Chem. Phys. **19**, 31982 (2017).
[35] B. Peng, H. Zhang, H. Shao, Y. Xu, R. Zhang, H. Lu, D. W. Zhang, and H. Zhu, ACS Appl. Mater. Inter. **8**, 20977 (2016).
[36] Y. Wang, N. Xu, D. Li, and J. Zhu, Adv. Funct. Mater. **27**, 1604134 (2016).
[37] A. Togo, L. Chaput, and I. Tanaka, Phys. Rev. B **91**, 094306 (2015).
[38] Y.-H. Lee, X.-Q. Zhang, W. Zhang, M.-T. Chang, C.-T. Lin, K.-D. Chang, Y.-C. Yu, J. T.-W. Wang, C.-S. Chang, L.-J. Li *et al.*, Adv. Mater. **24**, 2320 (2012).
[39] C. Lee, H. Yan, L. E. Brus, T. F. Heinz, J. Hone, and S. Ryu, ACS Nano **4**, 2695 (2010).
[40] V. Nicolosi, M. Chhowalla, M. G. Kanatzidis, M. S. Strano, and J. N. Coleman, Science **340**, 1226419 (2013).
[41] S. Zhao, Z. Li, and J. Yang, J. Am. Chem. Soc. **136**, 13313 (2014).
[42] S. Grimme, J. Antony, S. Ehrlich, and H. Krieg, J. Chem. Phys. **132**, 154104 (2010).
[43] S. Grimme, S. Ehrlich, and L. Goerigk, J. Comput. Chem. **32**, 1456 (2011).
[44] A. Tkatchenko and M. Scheffler, Phys. Rev. Lett. **102** 073005 (2009).
[45] T. Bučko, S. Lebègue, J. Hafner, and J. G. Ángyán, J. Chem. Theory Comput. **9**, 4293 (2013).
[46] T. Bučko, S. Lebègue, J. G. Ángyán, and J. Hafner, J. Chem. Phys. **141**, 034114 (2014).
[47] J. M. Skelton, D. Tiana, S. C. Parker, A. Togo, I. Tanaka, and A. Walsh, J. Chem. Phys. **143**, 064710 (2015).
[48] J. M. Skelton, L. A. Burton, F. Oba, and A. Walsh, J. Phys. Chem. C **121**, 6446 (2017).
[49] R. Zacharia, H. Ulbricht, and T. Hertel, Phys. Rev. B **69**, 155406 (2004).
[50] L. F. Huang, P. L. Gong, and Z. Zeng, Phys. Rev. B **90**, 045409 (2014).
[51] L. F. Huang and Z. Zeng, J. Appl. Phys. **113**, 083524 (2013).
[52] P.-F. Liu, T. Bo, Z. Liu, O. Eriksson, F. Wang, J. Zhao, and B.-T. Wang, J. Mater. Chem. C **6**, 12689 (2018).
[53] Y. Zhang, J. Materiomics **2**, 237 (2016).
[54] H. Shao, X. Tan, T. Hu, G. Q. Liu, J. Jiang, and H. Jiang, Europhys. Lett. **109**, 47004 (2015).
[55] B. Peng, D. Zhang, H. Zhang, H. Shao, G. Ni, Y. Zhu, and H. Zhu, Nanoscale **9**, 7397 (2017).
[56] B. Peng, H. Zhang, H. Shao, K. Xu, G. Ni, J. Li, H. Zhu, and C. M. Soukoulis, J. Mater. Chem. A **6**, 2018 (2018).
[57] B.-T. Wang, J.-J. Zheng, X. Qu, W.-D. Li, and P. Zhang, J. Alloy. Compd. **628**, 267 (2015).
[58] L. C. Zhang, G. Qin, W. Z. Fang, H. J. Cui, Q. R. Zheng, Q. B. Yan, and G. Su, Sci. Rep. **6**, 19830 (2016).
[59] D. Parker and D. J. Singh, Phys. Rev. B **82**, 035204 (2010).
[60] L. D. Zhao, H. J. Wu, S. Q. Hao, C. I. Wu, X. Y. Zhou, K. Biswas, J. Q. He, T. P. Hogan, C. Uher, C. Wolverton, V. P. Dravid, and M. G. Kanatzidis, Energy Environ. Sci. **6**, 3346 (2013).
[61] J. J. Pulikkotil, D. J. Singh, S. Auluck, M. Saravanan, D. K. Misra, A. Dhar, and R. C. Budhani, Phys. Rev. B **86**, 155204 (2012).
[62] X. Xu, J. Chen, and B. Li, J. Phys.: Condens. Matter. **28**, 483001 (2016).
[63] Y. Cai, J. Lan, G. Zhang, and Y.-W. Zhang, Phys. Rev. B **89**, 035438 (2014).